



Rapid Flame Doping of Co to WS₂ for Efficient Hydrogen Evolution

Journal:	<i>Energy & Environmental Science</i>
Manuscript ID	EE-ART-04-2018-001111.R1
Article Type:	Paper
Date Submitted by the Author:	18-May-2018
Complete List of Authors:	<p>Shi, Xinjian; Stanford University, Department of Mechanical Engineering, Fields, Meredith; Stanford University Park, Junsuk; Stanford University, Materials science and engineering McEnaney, Joshua; Stanford University, Chemical Engineering Yan, Hongping; Stanford University Zhang, Yirui; Massachusetts Institute of Technology Tsai, Charlie; Stanford University, Department of Chemical Engineering; SUNCAT Center for Interface Science and Catalysis, SLAC National Accelerator Laboratory, Jaramillo, Thomas; Stanford University, Assistant Professor of Chemical Engineering Sinclair, Robert; Stanford University, Materials Science and Engineering Nørskov, Jens; Stanford University, Chemical Engineering Zheng, Xiaolin; Stanford University,</p>

Rapid Flame Doping of Co to WS₂ for Efficient Hydrogen Evolution

Xinjian Shi^{1#}, Meredith Fields^{2#}, Joonsuk Park^{3#}, Joshua M. McEnaney², Hongping Yan^{2,4}, Yirui Zhang¹, Charlie Tsai², Thomas F. Jaramillo², Robert Sinclair³, Jens K. Nørskov^{2*}, Xiaolin Zheng^{1*}

1 Department of Mechanical Engineering, Stanford University, Stanford, California 94305, United States

2 Department of Chemical Engineering, Stanford University, Stanford, California 94305, United States

3 Department of Material Science and Engineering, Stanford University, Stanford, California 94305, United States

4 SLAC National Accelerator Laboratory, Menlo Park, California 94025, United States

These authors contribute equally to this work.

* Correspondence and requests for materials should be addressed to J.K.N (norskov@stanford.edu), or to X.Z (xlzheng@stanford.edu).

Abstract:

Transition metal sulfides have been widely studied as electrocatalysts for the hydrogen evolution reaction (HER). Though elemental doping is an effective way to enhance sulfide activity for HER, most studies have only focused on the effect of doping sulfide edge sites. Few studies have investigated the effect of doping the basal plane or the effect of doping concentration on basal plane activity. Probing the dopant concentration dependence of HER activity is challenging due to experimental difficulties in controlling dopant incorporation. Here, we overcome this challenge by first synthesizing doped transition metal oxides and then sulfurizing the oxides to sulfides, yielding core/shell Co-doped WS₂/W₁₈O₄₉ nanotubes with a tunable amount of Co. Our combined density functional theory (DFT) calculations and experiments demonstrate that the HER activity of basal plane WS₂ changes non-monotonically with the concentration of Co due to local changes in the binding energy of H and formation energy of S-vacancies. At an optimal Co doping concentration, the overpotential to reach -10 mA/cm² is reduced by 210mV, and the Tafel slope is reduced from 122 to 49 mV per decade (mV/dec) compared to undoped WS₂ nanotubes.

Introduction:

Developing cost-effective catalysts for the hydrogen evolution reaction (HER) will facilitate broader employment of water splitting for hydrogen production.¹⁻⁴ To replace state-of-the-art of Pt electrodes, many earth-abundant materials have been investigated as HER catalysts.⁵⁻⁷ In this context, transition metal sulfides, such MoS₂ and WS₂, remain one of the most studied subgroups of materials for HER.^{2, 8-10} Various approaches can be used to enhance the HER activity of transition metal sulfides, such as maximizing surface area through nanostructuring^{3, 11}, modifying charge density distribution and intrinsic electrocatalytic activity through vacancies manipulation¹² and chemical modification.^{2, 6} Among these approaches, incorporating various metal dopants, such as Co and Ni, improves the HER activity of sulfides.^{9, 13, 14} Most studies have focused on the effect of doping edge sites, with only a few reports on basal plane doping.¹⁵⁻²¹ These reports focused on the effect of dopant chemical composition. Little is known about the effect of doping concentration on HER activity due to the challenges associated with achieving controlled, variable dopant concentrations.

Herein, we overcome this challenge by first synthesizing doped transition metal oxides and then sulfurizing the oxides to sulfides. Specially, we first synthesized W₁₈O₄₉ nanotubes using flame vapor deposition²²⁻²⁴ and doped the surface of W₁₈O₄₉ nanotubes with cobalt (Co) using a sol-flame doping method.²⁵⁻²⁹ Finally, the doped nanotubes were sulfurized, forming Co doped tungsten sulfide/tungsten oxide (Co:WS₂/Co:W₁₈O₄₉) core/shell nanotubes. Our material characterization indicates that Co is incorporated into the WS₂ lattice, producing cobalt doped 2H-WS₂ nanotubes with stabilized 1T-WS₂ domains. Theoretical analysis indicates that Co doping modifies the H binding energy around S-active sites, improving the basal plane HER activity of both 2H and 1T-phase WS₂. The HER activity does not strictly increase with increasing Co doping concentration, which is supported by our experiments. By optimally doping the WS₂ sample, the overpotential to reach -10 mA/cm² is reduced by 210mV (from 0.45 V to 0.24 V vs. RHE), and the Tafel slope is reduced from 122 to 49 mV per decade (mV/dec).

Results and Discussion

Theoretical analyses

In previous studies, the HER activity of transition metal sulfide basal planes has been tuned via single-atom metal dopants.^{16, 17} Similarly for WS₂, when a Co atom substitutes a W atom in

the basal plane, changes in the local bond order of neighboring S atoms affect the hydrogen binding energy to these active sites. From an electronic structure perspective, this behavior has been attributed to the metal dopant atom's ability to introduce electronic states around the Fermi level of the semiconducting surface,¹⁶ mimicking the density of states seen for active unsaturated S-edges and enhancing H adsorption.

Achieving peak HER activity requires designing an active site which binds hydrogen neither too strongly nor too weakly. Based on this Sabatier principle, we predict there should exist an optimal amount of Co doping. Indeed, we find that the binding behavior of S-active sites strongly depends on the local doping configuration. The hydrogen binding energy to an S-active site changes non-monotonically with increasing Co concentration (Figure S1). We use density functional theory (DFT) to model the electronic influence of Co doping for an idealized 4x4 2H-WS₂ unit cell and 4x4 1T-WS₂ unit cell. We first determined the most stable (*i.e.*, the lowest energy) dopant configurations for increasing ratios of Co:W (Figure 1a and 1b, left columns). The incorporation of Co into the WS₂ lattice is an endergonic process according to calculated formation energies (Table S1), indicating that very high doping concentrations are thermodynamically unfavorable. The Co dopant atoms tend to aggregate in clusters to lower the system energy (Figure 1a and 1b, "Geometry", Co atoms: pink). For both Co-doped 2H and 1T-phase WS₂, hydrogen tends to preferentially adsorb on the S-sites neighboring the Co dopant. Although in many density functional theory (DFT) studies, the minimum free energy of H adsorption across the surface (the binding energy associated with a single lowest energy site) is used as the sole thermodynamic indicator of HER activity, here we also show the evolution in binding behavior of the surface as a whole. Figure 1 a and b "Activity Map" shows a color map of changing H binding energies (ΔG_H) to each S-active site for increasingly doped surfaces. Dark blue corresponds to weak H adsorption, red corresponds to strong H adsorption and yellow corresponds to the optimal range for H adsorption (Figure 1, middle color scale bar). As more Co atoms (pink) replace W atoms, the H binding energy shifts to increasingly orange exergonic values (such as a minimum ΔG_H of -0.98 eV seen in the 13% atomic percentage of Co doping case), before transitioning to increasingly blue endergonic values (25% Co and above). Figure 1 also indicates that the effects of doping are often local, with a Co dopant tuning the binding behavior of its nearest sulfur neighbors.

Figure 1c and d show the minimum ΔG_H values across the 4x4 unit cell as a function of atomic percentage of Co for 2H and 1T-phase of WS₂, respectively. For both phases, the value of

the lowest ΔG_H first decreases and then increases with increasing Co concentration. Adding a Co dopant atom increases the favorability of H binding to the S-active site, and then with increasing dopant concentrations, this relationship slowly weakens to yield deactivated basal planes. In both cases, the doping configurations leading to optimal HER activity are very specific and occur over a narrow concentration range. Figure 1c and d reveal that across all considered surfaces, the best ΔG_H is -0.05 eV for the 1T phase surface at 13% doping (2 Co atoms per unit cell) and -0.12 eV at a concentration of 6% for the 2H phase (1 Co atom per unit cell). Both pristine and doped 1T-phase WS_2 are more active for HER than the 2H-phase WS_2 .

Since the Co: WS_2 surface may contain S-vacancies that can also contribute to HER activity in our experiments,³⁰⁻³² we calculated the effect of basal plane Co doping on S-vacancy formation. The S-vacancy calculations were performed for the most stable Co-doped surfaces. S-vacancy formation becomes more favorable with increasing local Co-dopant concentration, shown by the positive values of the vacancy formation energy (Figure S2a). At higher doping concentrations, introducing sulfur defects creates binding sites with comparable adsorption energies to the best-case defect-free surface. The structure with a ΔG_H closest to 0 occurs for a 3-fold Co-doped S-vacancy with a value of -0.1 eV (Figure S2b, 19% Co).

Our calculations suggest that precise control of transition metal doping in sulfide lattices can fine tune the activity of basal planes for HER. Active site binding is a strong function of local doping structure, and more is not always better. Both Co-doping and S-vacancy formation alter the binding properties of the surface. Ideal basal plane configuration of WS_2 for peak HER activity correspond to either isolated Co-dopant domains or defect-rich domains at higher local Co concentrations.

Experimentally, the true WS_2 nanotube surface is a complex combination of a variety of doped and defect modified active sites, and each contributes to the overall turnover rate. The experimental determined HER activity is also a convolution of differing Co concentrations at the inner and outer nanotube walls, the presence of polycrystalline domains, and co-existence of 1T and 2H phases. Therefore, a strict correspondence is not anticipated between the experimental value and theoretical value for the optimal dopant concentration. However, DFT calculations reaffirm the hypothesis that decreased overpotential with Co incorporation may in part be attributed to activation of inert basal plane sites. Furthermore, decreased activity could be expected with higher doping concentrations, related to the formation of clustered Co-dopant sites which bind hydrogen too strongly.

Experimental results

Figure 2 schematically illustrates the synthesis process of Co:WS₂. We first synthesized W₁₈O₄₉ nanotubes on FTO glass substrates using flame vapor deposition. The flame oxidizes tungsten wires to tungsten oxide vapor and condenses the vapor onto FTO glass, forming W₁₈O₄₉ nanotubes. Then, we doped the W₁₈O₄₉ nanotubes with Co using the sol-flame doping method.²⁵⁻²⁷ The sol-flame doping method requires dip-coating the nanotubes in a Co precursor solution, followed by rapid high temperature annealing (1100°C for 2 mins) and fast cooling. The concentration of Co dopants is increased by increasing the Co precursor concentration and/or repeating the dip-coating procedure.^{27, 29} Finally, the Co-doped W₁₈O₄₉ is sulfurized to Co-doped WS₂. The final nanotubes (Figure 2, right) are Co:WS₂ shells (higher Co doping concentration) and Co:W₁₈O₄₉ cores (lower Co doping concentration). The Co dopant concentration is higher on the surface and gradually decreases with depth. Both the outer and inner surface are catalytic active for HER. The core Co:W₁₈O₄₉ exhibits metallic properties and serves as a conductive pathway for charge transport.³³⁻³⁷ As a control sample, we also prepared WS₂/W₁₈O₄₉ core/shell nanotubes without conducting the doping step.

Figures 3a-c show the corresponding scanning electron microscopy (SEM) images of pristine W₁₈O₄₉, Co:W₁₈O₄₉, and Co:WS₂/Co:W₁₈O₄₉ nanotubes illustrated in Figure 2. All three types of nanotubes show similar morphologies, with an average length of 2.5 μm and diameter of 90 nm, indicating that both sol-flame doping and sulfurization processes have little impact on the morphology. This allows us to isolate the effect of Co doping on the nanotube HER activity. The hollow nanotube structure is confirmed by close inspection of a single Co:WS₂/Co:W₁₈O₄₉ nanotube (Figure S3 a and b). Grazing-incidence wide-angle x-ray scattering (GIWAXS) results show that Co:WS₂/Co:W₁₈O₄₉ nanotubes have nearly identical but slightly shifted peaks along the larger scattering wave vector Q compared to pristine WS₂/W₁₈O₄₉ (Figure 3d). This common shift indicates that Co atoms substitute W atoms in the WS₂/W₁₈O₄₉ lattice, resulting in smaller d-spacing ($d_{\text{spacing}} = 2\pi/Q$). If the Co atoms instead occupied interstitial sites, this would be indicated by a set of X-ray diffraction peaks associated with a disrupted or alternate crystal structure. The substitution of Co into the W lattice prohibits the formation of cobalt oxide and subsequent cobalt sulfide (CoS₂) after sulfurization. The formation of Co:WS₂ instead of CoS₂ after sulfurization is also supported by the significant HER performance difference with the CoS₂

case discussed later (Fig. 5d). High resolution transmission electron microscopy (HRTEM) images in Figure 3e (edge) and 3f (cross-section) show that the nanotube has an outer diameter of 90nm and inner diameter of 30nm. Figure 3e shows that the Co:WS₂ layer is only a couple of atomic layers thick and has a lattice spacing of 0.62nm. The flatness of the Co:WS₂ layer indicates the Co atoms are effectively doped instead of forming cobalt oxide based on our previous studies on the morphology control of the sol-flame method.^{25, 28, 29} The inner core is Co:W₁₈O₄₉ with a lattice spacing of 0.38nm. The presence of a thin WS₂ shell is also confirmed by Fast Fourier transform (FFT) and inverse FFT analysis (Figure S3c and d), as well as by the scanning TEM-high angle annular dark field (STEM-HAADF) image shown in Figure S3e and f. The spatial distribution of Co in the nanotube is determined by energy dispersive X-ray spectroscopy (EDS) and electron energy loss spectroscopy (EELS). Figure 3g shows the atomic percentages of W, Co, S and O at six positions as marked in Figure 3f. The atomic percentage of W is uniform across the nanotube. The atomic percentages of Co and S are higher near the outer and inner surfaces (Co/(W+Co) ~ 15%). Such spatial distribution of Co matches well with the EELS line scanning measurement (Figure 3h, red curve), where an STEM image is used as the background to mark the line scanning positions for the EELS result. The combined EDS and EELS measurements confirm that we have successfully synthesized Co:WS₂/Co:W₁₈O₄₉ nanotubes.

The Raman and X-ray photoelectron spectra (XPS) of the Co:WS₂/Co:W₁₈O₄₉ (for the most active sample) are shown in Figure 4. The Raman data in Figure 4a illustrate that the characteristic WS₂ peaks are submerged within the main W₁₈O₄₉ peak, confirming that the WS₂ layer is very thin. The XPS spectra of W 4f peaks (Figure 4b) show the co-existence of W⁴⁺ valence for WS₂ and W⁵⁺ and W⁶⁺ valences for W₁₈O₄₉. The XPS measurement also confirms the existence of S (Figure 4c) and Co (Figure 4d) elements in the nanotubes. The XPS Co 2p peak intensity increases with increasing the Co doping precursor concentrations and/or coating times (Figure S4). The integrated Co 2p peak area ratio is used to estimate the surface Co concentration, and is referenced to the Co 2p_{3/2} of the 15% Co-doped sample (concentration determined by EDS (Figure 3g). Doping condition: twice coated in 0.20M Co precursor). The fitted curves for XPS S 2p peaks reveal that Co:WS₂ consists of both the 2H-phase and 1T-phase.³⁸⁻⁴⁰ The co-existence of two phases is consistent with a previous study which shows that doping can lead to the formation of the more active 1T-phase of WS₂.⁴¹

Next, we conducted electrochemical measurements to quantify the effect of Co concentration on the HER activity of Co:WS₂/Co:W₁₈O₄₉ nanotubes on fluorine doped tin oxide (FTO). Figure 5a shows the current density (based on geometric area of FTO substrate) vs. potential curves for the undoped pristine WS₂/W₁₈O₄₉ (0%), mildly doped (10%), and optimally doped (15%) Co:WS₂/Co:W₁₈O₄₉ nanotubes. The Co atomic percentage at the outer surface of nanotube is used to label different conditions. The dashed and solid lines correspond to before and after iR correction. Figure 5b plots the corresponding Tafel plots. Tafel results clearly show that Co doping enhances the HER activity of WS₂. For example, the optimally doped sample (15%) reduces the onset potential for achieving -10mA/cm² by 210 mV and reduces the Tafel slope from 122 mV/dec to 49 mV/dec. We tested the HER activity of the nanotubes with different growth times, different Co precursor concentrations (Figure S5), and different dip-coating times and sulfurization times (Figure S6). We confirmed that the enhancement effect of Co doping does not depend on the nanotube growth time, but depends mainly on the doping concentration (Figure S5). Figure 5c plots the overpotential for achieving -10mA/cm² as a function of the surface Co doping concentration. Clearly, the overpotential first decreases and then slightly increases with increasing the Co doping concentration, supporting the hypothesis that there should be an optimal Co doping concentration. The stability tests were performed for both undoped WS₂ and optimally doped Co:WS₂ with a Cyclic voltammetry scan of 1000 cycles (Figure S7a). For both samples, their J-V curves show very small changes, indicating good stabilities.

Table 1 compares the HER activity of our WS₂ and Co:WS₂ nanotubes versus various forms of WS₂ in the literature. The chemical composition and substrate surface area affect the HER performance dramatically. For fair comparison, Table 1 only summarizes the HER activity of WS₂ on FTO^{10, 40, 42-45}. The table shows that our Co:WS₂ achieves the highest current density at -0.4V vs. RHE, demonstrating the benefit of appropriate Co doping. We also compare Co doping of WS₂ with other doped sulfides, and the results are summarized in Table S2.⁴⁶⁻⁵² While WS₂ is not the best HER catalyst compared to other transition metal sulfides, and the corresponding overpotential associated with Co:WS₂ is not the lowest, we do find that tuning dopant concentration allows us to maximize the reduction in overpotential compared to all other catalysts sampled. This holds true even in cases where alternate substrates are used.

Finally, since both WS_2 and cobalt sulfide CoS_2 are active for HER, we need to compare their HER activities against Co:WS_2 . In the literature, there are several reports of excellent HER performance for both CoS_2 and WS_2 .⁵³⁻⁵⁵ We cannot directly compare the activities of these samples to our Co:WS_2 nanotubes due to morphological and substrate differences. Instead, we coated CoS_2 shells onto $\text{W}_{18}\text{O}_{49}$ nanotubes for a consistent comparison to our WS_2 and Co:WS_2 samples. The synthesis procedure of $\text{CoS}_2/\text{W}_{18}\text{O}_{49}$ nanotubes is similar to that described in Figure 2, except that the high temperature flame annealing (1100°C for 2 mins) is replaced by a low temperature furnace annealing (300°C for 2hrs). The low temperature annealing allows the growth of Co oxide before sulfurization.²⁹ Figure 5d compares the overpotential for achieving $-10\text{mA}/\text{cm}^2$ for WS_2 , Co:WS_2 and CoS_2 shells on $\text{W}_{18}\text{O}_{49}$ nanotubes, and the corresponding $J-V$ curves are shown in Figure S7b. The Co:WS_2 sample is more active than both pristine WS_2 and CoS_2 samples, suggesting a synergistic combination of Co, W and S can optimally tune the HER activity compared to undoped Co or W based sulfide systems.

Conclusions

In summary, we combine theoretical analysis and experimental verification to investigate the effect of Co doping concentration on the basal plane activity of WS_2 for HER. Our DFT calculations suggest that precise control of Co doping in both 2H and 1T-phase WS_2 lattices can fine tune the activity of basal planes for HER. Active site H-binding is a strong function of local doping structure, and more is not always better. In the case of WS_2 , the basal plane active sites with an optimal H-binding energy are either S sites adjacent to isolated Co dopants, or S-vacancy sites in the presence of Co-rich domains. Experimentally, we synthesized undoped and Co-doped $\text{WS}_2/\text{W}_{18}\text{O}_{49}$ core/shell nanotubes using flame synthesis and a sol-flame doping process. This method overcomes challenges associated with doping sulfide basal planes by first doping a metal oxide and then converting the oxide to a sulfide through sulfurization. The true Co:WS_2 surface contains both 1T and 2H-phases and a variety of possible doped and defect surface structures; all of these variations contribute to the overall turnover rate. Despite these complexities, the HER activity of the basal plane Co:WS_2 does increase and then decrease with increasing the concentration of the Co dopants. This finding is consistent with theoretical calculations which show that dopant-improved HER activity is only expected within a narrow concentration range. The optimal Co doping concentration (15 atomic % for WS_2) yields a substantial reduction in

overpotential (~ 210 mV reduction to achieve -10 mA/cm²). This reduction is superior to results for other various doped sulfides, where overpotential shifts range from $50 \sim 200$ mV. Finally, we find that Co:WS₂ is more active for HER than both pristine WS₂ and CoS₂ nanotubes, suggesting a synergistic combination of Co, W and S can optimally tune the hydrogen binding energy and yield improved HER activity.

Methods

Experimental Details

1. Synthesis of tungsten oxide nanotubes

The synthesis of tungsten oxide (W₁₈O₄₉) nanotubes includes two steps: 1) seed layer synthesis and 2) flame vapor deposition. The basic procedures follow those previously reported in Rao et al.²² In this study, we lower the FTO substrate temperature from 550°C to 500°C to grow hollow nanotubes instead of nanowires.

2. Cobalt doping

The Co doping method for W₁₈O₄₉ nanotubes follows previous reports.²⁹ The Co precursors are cobalt acetate tetrahydrate (Co(CH₃COO)₂·4H₂O, 99%, Aldrich) dissolved in 2-methoxyethanol (C₃H₈O₂, >99%, Acros Organics) with concentrations of 0.02M, 0.08M, 0.14M, 0.20M and 0.26M. The as-deposited W₁₈O₄₉ sample was dipped into the prepared cobalt precursor and withdrawn at a constant speed of 1.0 mm/s at ambient temperature and pressure. The samples were allowed to dry in a fume hood. Flame annealing was conducted at 1100°C for 2 mins, followed by fast room temperature cooling process. To achieve higher Co doping concentration, the dipping and doping processes are repeated either twice or three times.

3. Sulfurization

The as-fabricated Co:W₁₈O₄₉ nanotubes were sulfurized in a quartz tube furnace at 250°C for 1hr, 2hr, and 3hrs in a mixed H₂S/H₂ (1:9 volume ratio) atmosphere, and the HER performance results in Figure S6b show that 2hr is the optimal condition. The sample was heated from room temperature to 250°C with a $5^{\circ}\text{C}/\text{min}$ ramp rate. Thus, the outer surface of Co:W₁₈O₄₉ is converted to Co:WS₂, forming Co:WS₂/Co:W₁₈O₄₉ core/shell nanotubes.

Material Characterization

Raman spectra were measured using the Horiba Labram Raman, equipped with the HORIBA Scientific LabRAM HR Evolution spectrometer and AIST-NT's SmartSPM Scanning Probe Microscope. Morphology analyses of the samples were carried out using a scanning electron microscope (FEI XL30 Sirion SEM with FEG source), and a transmission electron microscope (FEI Titan environmental TEM 80-300) equipped with a spherical aberration (Cs) image corrector, Gatan Quantum 966 EEL spectrometer and Oxford Xmax SDD EDS Detector. The X-ray photoelectron spectroscopy (XPS) measurements were carried out using a PHI VersaProbe 1 Scanning XPS Microprobe. The grazing-incidence wide-angle X-ray scattering (GIWAXS) measurement was done at beamline 11-3 of Stanford Synchrotron Radiation Lightsource (SSRL) at SLAC National Accelerator Laboratory (SLAC), with a fixed X-ray photon energy (12.7 keV), which is equipped with a two-dimensional Rayonix MX225 CCD area detector. The sample-detector distance was ~125 mm, and the incident angle was 2 degrees to ensure sufficient sampling of the nanotube samples on the substrate. The 2-dimensional GIWAXS data were reduced to a scattering profile using NIKA package with Igor Pro software⁵⁶ and WAXS tools.⁵⁷

Electrochemical Measurement

The electrochemical measurement was conducted in a three-electrode system with 0.5M H₂SO₄ as the electrolyte, using nanotubes on FTO as the working electrode, carbon cloth and Ag/AgCl as the counter and reference electrodes, respectively.

Theoretical calculations

Plane-wave DFT calculations employing ultrasoft pseudopotentials were performed using the Quantum ESPRESSO suite⁵⁸ and the Atomic Simulation Environment (ASE) interface.⁵⁹ The BEEF-vdW⁶⁰ exchange correlation functional was implemented with ultrasoft pseudopotentials,⁶¹ plane-wave and density cutoffs set to 500 and 5000 eV, respectively, with a Fermi smearing width of 0.1 eV and (4×4×1) k-point sampling.⁶² Periodic boundary conditions with dipole corrections were invoked, with 10 Å of vacuum set between neighboring slabs in the z direction. For further information on calculated binding and formation energies, refer to supplementary information.

Author contributions

X.Z., J.K.N., X.S. and M.F. conceived the idea and designed the research plan. X.S performed the majority of the experiments. M. F. conducted the DFT simulation and theoretical analyses. J.P. conducted TEM measurements and related analyses under supervision of R.S; J.M.M performed the sulfurization process under supervision of T.F.J.; H.Y. performed the GIWAXS analyses. Y.Z. assisted on experiments and data summary. C.T. assisted on theoretical analyses. X.S. M.F. and J.P. prepared the draft, and X. Z. and J.K.N. supervised the project. All the authors discussed the results and contributed to the final manuscript.

Conflicts of interest

There are no competing interest to declare.

Acknowledgements

X. Zheng acknowledges the support by Stanford Precourt Institute for Energy and Stanford Natural Gas Initiative. M. Fields acknowledges a graduate fellowship through the National Science Foundation. Part of this work was performed at the Stanford Nano Shared Facilities (SNSF), supported by the National Science Foundation under award ECCS-1542152. Use of the Stanford Synchrotron Radiation Light source, SLAC National Accelerator Laboratory, was supported by the U.S. Department of Energy, Office of Science, and Office of Basic Energy Sciences under contract no. DE-AC02-76SF00515. We also thank Tim J. Dunn and Kevin H. Stone for assistance during the GIWAXS experiment at SSRL Beamline 11-3.

References:

1. A. Lasia, *Handbook of fuel cells*, 2010.
2. Y. Li, H. Wang, L. Xie, Y. Liang, G. Hong and H. Dai, *Journal of the American Chemical Society*, 2011, **133**, 7296-7299.
3. E. J. Popczun, J. R. McKone, C. G. Read, A. J. Biacchi, A. M. Wiltrout, N. S. Lewis and R. E. Schaak, *Journal of the American Chemical Society*, 2013, **135**, 9267-9270.
4. D. Voiry, M. Salehi, R. Silva, T. Fujita, M. Chen, T. Asefa, V. B. Shenoy, G. Eda and M. Chhowalla, *Nano letters*, 2013, **13**, 6222-6227.
5. D. Kong, H. Wang, Z. Lu and Y. Cui, *Journal of the American Chemical Society*, 2014, **136**, 4897-4900.
6. M. Cabán-Acevedo, M. L. Stone, J. Schmidt, J. G. Thomas, Q. Ding, H.-C. Chang, M.-L. Tsai, J.-H. He and S. Jin, *Nature Materials*, 2015.
7. P. D. Tran, S. K. Batabyal, S. S. Pramana, J. Barber, L. H. Wong and S. C. J. Loo, *Nanoscale*, 2012, **4**, 3875-3878.
8. Y. Yan, B. Xia, Z. Xu and X. Wang, *ACS Catalysis*, 2014, **4**, 1693-1705.
9. H. Wang, C. Tsai, D. Kong, K. Chan, F. Abild-Pedersen, J. K. Nørskov and Y. Cui, *Nano Research*, 2015, **8**, 566-575.
10. R. Morrish, T. Haak and C. A. Wolden, *Chemistry of Materials*, 2014, **26**, 3986-3992.
11. J. Y. Kim, H. Kim, B. H. Kim, T. Chang, J. Lim, H. M. Jin, J. H. Mun, Y. J. Choi, K. Chung and J. Shin, *Nature communications*, 2016, **7**, 12911.
12. F. Li, X. Zhao, J. Mahmood, M. S. Okyay, S.-M. Jung, I. Ahmad, S.-J. Kim, G.-F. Han, N. Park and J.-B. Baek, *ACS nano*, 2017, **11**, 7527-7533.
13. P. Zhang, T. Wang and J. Gong, *Advanced Materials*, 2015, **27**, 5328-5342.
14. T. Arai, S.-i. Senda, Y. Sato, H. Takahashi, K. Shinoda, B. Jeyadevan and K. Tohji, *Chemistry of Materials*, 2008, **20**, 1997-2000.
15. T. Palaniselvam and J.-B. Baek, *2D Materials*, 2015, **2**, 032002.
16. J. Deng, H. Li, J. Xiao, Y. Tu, D. Deng, H. Yang, H. Tian, J. Li, P. Ren and X. Bao, *Energy & Environmental Science*, 2015, **8**, 1594-1601.
17. Y. Qu, H. Pan, C. T. Kwok and Z. Wang, *Nanoscale research letters*, 2015, **10**, 480.
18. G. Gao, Q. Sun and A. Du, *The Journal of Physical Chemistry C*, 2016, **120**, 16761-16766.

19. D. Gao, B. Xia, C. Zhu, Y. Du, P. Xi, D. Xue, J. Ding and J. Wang, *Journal of Materials Chemistry A*, 2018, **6**, 510-515.
20. P. Liu, J. Zhu, J. Zhang, K. Tao, D. Gao and P. Xi, *Electrochimica Acta*, 2018, **260**, 24-30.
21. W. Xiao, P. Liu, J. Zhang, W. Song, Y. P. Feng, D. Gao and J. Ding, *Advanced Energy Materials*, 2017, **7**.
22. P. M. Rao, L. Cai, C. Liu, I. S. Cho, C. H. Lee, J. M. Weisse, P. Yang and X. Zheng, *Nano letters*, 2014, **14**, 1099-1105.
23. P. M. Rao, I. S. Cho and X. Zheng, *Proceedings of the Combustion Institute*, 2013, **34**, 2187-2195.
24. P. M. Rao and X. Zheng, *Proceedings of the Combustion Institute*, 2011, **33**, 1891-1898.
25. R. Luo, I. S. Cho, Y. Feng, L. Cai, P. M. Rao and X. Zheng, *Nanoscale research letters*, 2013, **8**, 347.
26. I. S. Cho, C. H. Lee, Y. Feng, M. Logar, P. M. Rao, L. Cai, D. R. Kim, R. Sinclair and X. Zheng, *Nat Commun*, 2013, **4**, 1723.
27. Y. Feng, I. S. Cho, P. M. Rao, L. Cai and X. Zheng, *Nano letters*, 2012, **13**, 855-860.
28. Y. Feng, I. S. Cho, L. Cai, P. M. Rao and X. Zheng, *Proceedings of the Combustion Institute*, 2013, **34**, 2179-2186.
29. L. Cai, I. S. Cho, M. Logar, A. Mehta, J. He, C. H. Lee, P. M. Rao, Y. Feng, J. Wilcox and F. B. Prinz, *Physical Chemistry Chemical Physics*, 2014, **16**, 12299-12306.
30. H. Li, M. Du, M. J. Mleczko, A. L. Koh, Y. Nishi, E. Pop, A. J. Bard and X. Zheng, *Journal of the American Chemical Society*, 2016, **138**, 5123-5129.
31. H. Li, C. Tsai, A. L. Koh, L. Cai, A. W. Contryman, A. H. Fragapane, J. Zhao, H. S. Han, H. C. Manoharan and F. Abild-Pedersen, *Nature materials*, 2016, **15**, 48-53.
32. C. Tsai, H. Li, S. Park, J. Park, H. S. Han, J. K. Nørskov, X. Zheng and F. Abild-Pedersen, *Nature communications*, 2017, **8**, 15113.
33. F. Mehmood, R. Pachter, N. R. Murphy, W. E. Johnson and C. V. Ramana, *Journal of Applied Physics*, 2016, **120**, 233105.
34. M. Vasilopoulou, I. Kostis, N. Vourdas, G. Papadimitropoulos, A. Douvas, N. Boukos, S. Kennou and D. Davazoglou, *The Journal of Physical Chemistry C*, 2014, **118**, 12632-12641.
35. M. Gillet, C. Lemire, E. Gillet and K. Aguir, *Surface Science*, 2003, **532**, 519-525.

36. F. Wang, C. Di Valentin and G. Pacchioni, *Physical Review B*, 2011, **84**, 073103.
37. R. Chatten, A. V. Chadwick, A. Rougier and P. J. Lindan, *The Journal of Physical Chemistry B*, 2005, **109**, 3146-3156.
38. T. Wang, C. Liu, F. Jiang, Z. Xu, X. Wang, X. Li, C. Li, J. Xu and X. Yang, *Physical Chemistry Chemical Physics*, 2017, **19**, 17560-17567.
39. K. Yang, X. Wang, H. Li, B. Chen, X. Zhang, S. Li, N. Wang, H. Zhang, X. Huang and W. Huang, *Nanoscale*, 2017, **9**, 5102-5109.
40. H. Zhou, F. Yu, J. Sun, R. He, Y. Wang, C. F. Guo, F. Wang, Y. Lan, Z. Ren and S. Chen, *Journal of Materials Chemistry A*, 2016, **4**, 9472-9476.
41. A. N. Enyashin, L. Yadgarov, L. Houben, I. Popov, M. Weidenbach, R. Tenne, M. Bar-Sadan and G. Seifert, *The Journal of Physical Chemistry C*, 2011, **115**, 24586-24591.
42. L. Yang, X. Wu, X. Zhu, C. He, M. Meng, Z. Gan and P. K. Chu, *Applied Surface Science*, 2015, **341**, 149-156.
43. J. Duan, S. Chen, B. A. Chambers, G. G. Andersson and S. Z. Qiao, *Advanced Materials*, 2015, **27**, 4234-4241.
44. C. L. Choi, J. Feng, Y. Li, J. Wu, A. Zak, R. Tenne and H. Dai, *Nano Research*, 2013, **6**, 921-928.
45. X. Xu, Y. Liu, Y. Zhu, X. Fan, Y. Li, F. Zhang, G. Zhang and W. Peng, *ChemElectroChem*, 2017.
46. D. Wang, X. Zhang, Y. Shen and Z. Wu, *RSC Advances*, 2016, **6**, 16656-16661.
47. X. Dai, K. Du, Z. Li, M. Liu, Y. Ma, H. Sun, X. Zhang and Y. Yang, *ACS applied materials & interfaces*, 2015, **7**, 27242-27253.
48. J. He, Y. Liang, J. Mao, X. Zhang, X. Yang, Z. Cui, S. Zhu, Z. Li and B. Li, *Journal of The Electrochemical Society*, 2016, **163**, H299-H304.
49. S.-Y. Huang, D. Sodano, T. Leonard, S. Luiso and P. S. Fedkiw, *Journal of The Electrochemical Society*, 2017, **164**, F276-F282.
50. N. Yang, C. Tang, K. Wang, G. Du, A. M. Asiri and X. Sun, *Nano Research*, 2016, **9**, 3346-3354.
51. C. Sun, J. Zhang, J. Ma, P. Liu, D. Gao, K. Tao and D. Xue, *Journal of Materials Chemistry A*, 2016, **4**, 11234-11238.
52. T. A. Shifa, F. Wang, K. Liu, Z. Cheng, K. Xu, Z. Wang, X. Zhan, C. Jiang and J. He, *Small*, 2017, **13**.

53. S. Ahn, J. Yang, H. Lim and H. S. Shin, *Nano convergence*, 2016, **3**, 5.
54. D. Voiry, H. Yamaguchi, J. Li, R. Silva, D. C. Alves, T. Fujita, M. Chen, T. Asefa, V. B. Shenoy and G. Eda, *Nature materials*, 2013, **12**, 850.
55. R. Bose, Z. Jin, S. Shin, S. Kim, S. Lee and Y.-S. Min, *Langmuir*, 2017, **33**, 5628-5635.
56. J. Ilavsky, *Journal of Applied Crystallography*, 2012, **45**, 324-328.
57. S. D. Oosterhout, V. Savikhin, J. Zhang, Y. Zhang, M. A. Burgers, S. R. Marder, G. C. Bazan and M. F. Toney, *Chemistry of Materials*, 2017, **29**, 3062-3069.
58. Q. Espresso, *J. Phys.: Condens. Matter*, 2009, **21**, 395502.
59. S. R. Bahn and K. W. Jacobsen, *Computing in Science & Engineering*, 2002, **4**, 56-66.
60. J. Wellendorff, K. T. Lundgaard, A. Møgelhøj, V. Petzold, D. D. Landis, J. K. Nørskov, T. Bligaard and K. W. Jacobsen, *Physical Review B*, 2012, **85**, 235149.
61. D. Vanderbilt, *Physical Review B*, 1990, **41**, 7892.
62. H. J. Monkhorst and J. D. Pack, *Physical review B*, 1976, **13**, 5188.

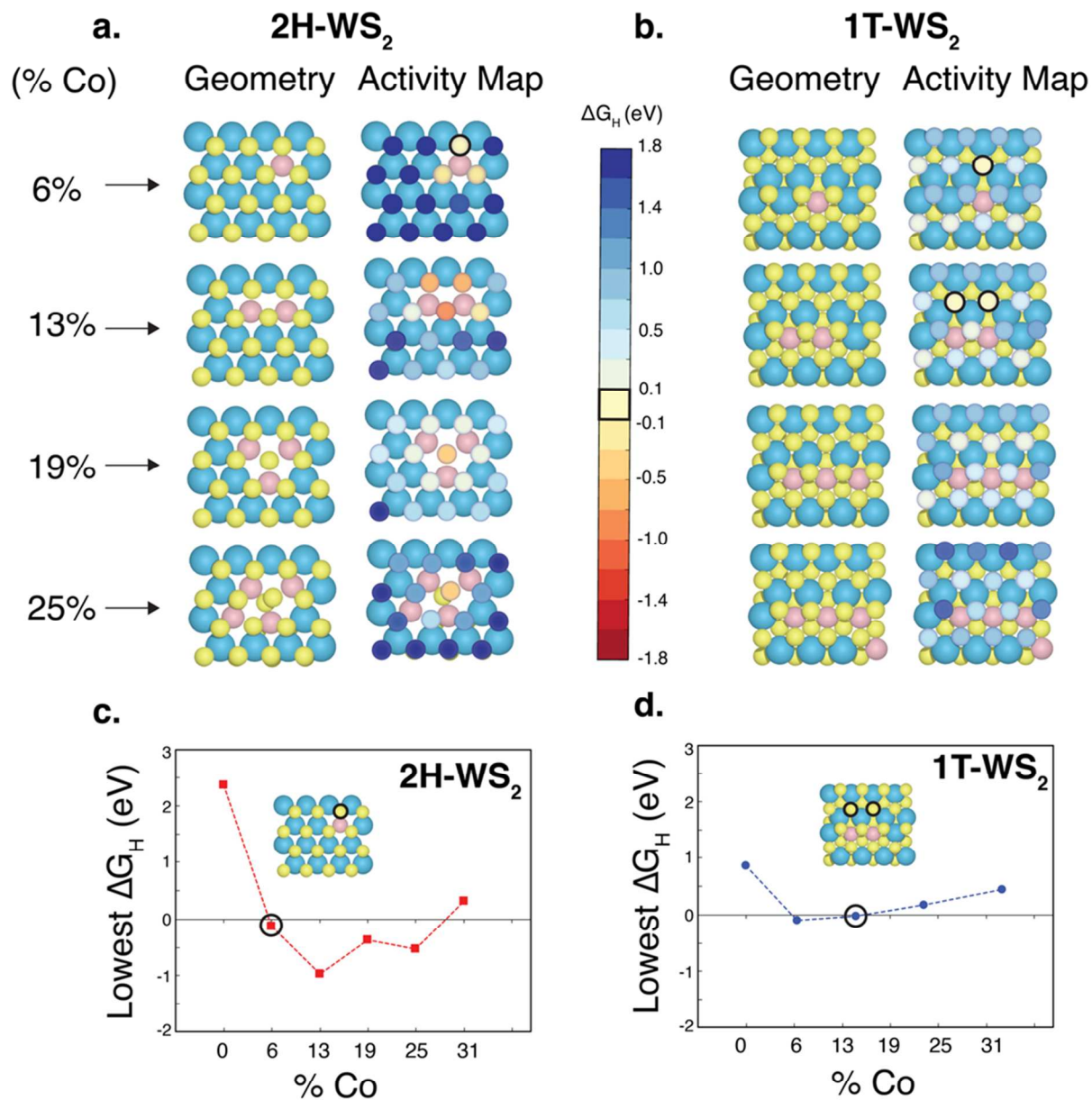


Figure 1. Free energy of Hydrogen Adsorption (ΔG_H) to 2H- and 1T- WS₂ with increasing Co-dopant concentration. Stable geometry (left, W in turquoise, Co in light pink, and S in yellow) and colored ΔG_H activity map (right) for a 4x4 (a) 2H-phase and (b) 1T-phase WS₂ basal planes as a function of Co doping concentration. Plot of the minimum ΔG_H across the basal plane for (c) 2H-WS₂ and (d) 1T-WS₂ as a function of doping concentration.

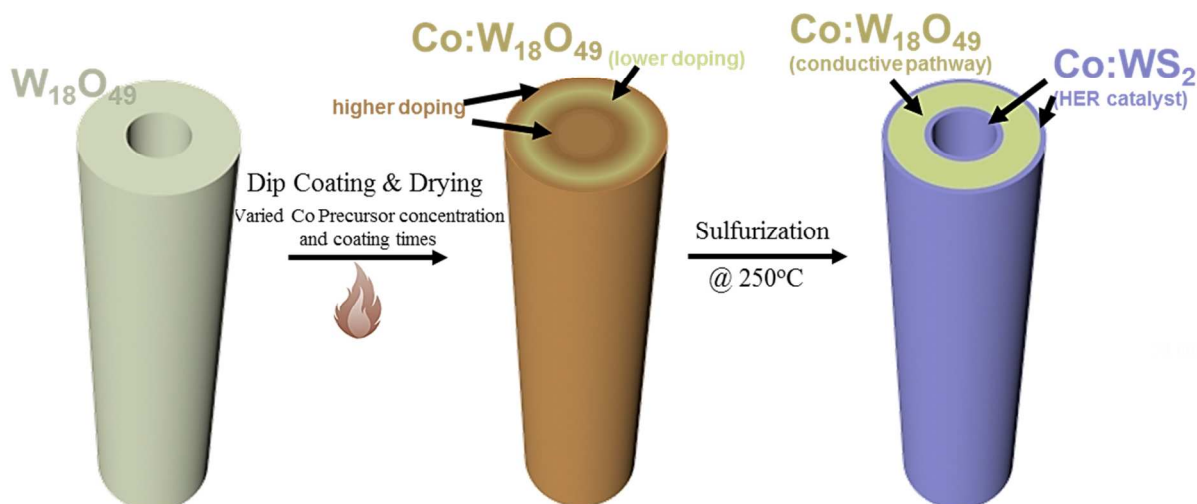


Figure 2. Schematic for the synthesis steps for Co:WS₂/Co:W₁₈O₄₉ core/shell nanotubes. First, W₁₈O₄₉ nanotubes were synthesized by flame vapor deposition (FVD) method. Second, Co was doped into W₁₈O₄₉ nanotubes using the sol-flame doping method, which involves dip-coating nanotubes with Co precursor, followed by rapid high flame annealing (1100 °C for 2min) and fast cooling. Finally, the surface of Co:W₁₈O₄₉ nanotubes were converted to sulfide by a low temperature sulfurization process (250 °C for 2hr), producing Co:WS₂/Co:W₁₈O₄₉ core/shell nanotubes.

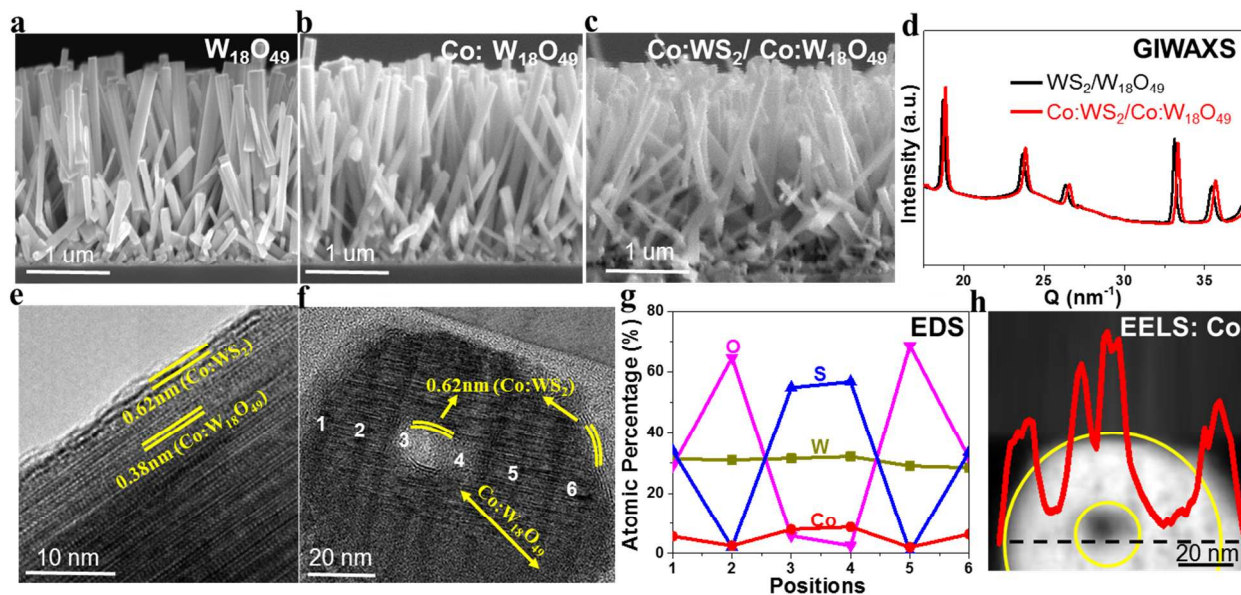


Figure 3: Material characterization of Co:WS₂/Co:W₁₈O₄₉ core/shell nanotubes. (a-c) SEM images show that pristine W₁₈O₄₉, Co:W₁₈O₄₉ and Co:WS₂/Co:W₁₈O₄₉ have similar morphology; (d) GIWAXS spectra of WS₂/W₁₈O₄₉ (black) and Co:WS₂/Co:W₁₈O₄₉ (red). The two spectrum have nearly identical peaks with a slight shift, indicating the Co atom substitution to W atom; (e) HRTEM image shows that the surface 2-3 atomic layers are Co:WS₂ and the inside is Co:W₁₈O₄₉; (f) HRTEM image of the cross section of one single nanotube from focused ion beam (FIB) cutting, where numbers 1 to 6 indicate positions for EDS measurement of W, S, Co, O atomic percentage with results in (g); (g) the atomic percentage of each element at each position, in which Co:(Co+W) at the nanotube outer surface is ~15%; (h) EELS data of cobalt along the black dash line of the nanotube. The background STEM image labels the positions for EELS.

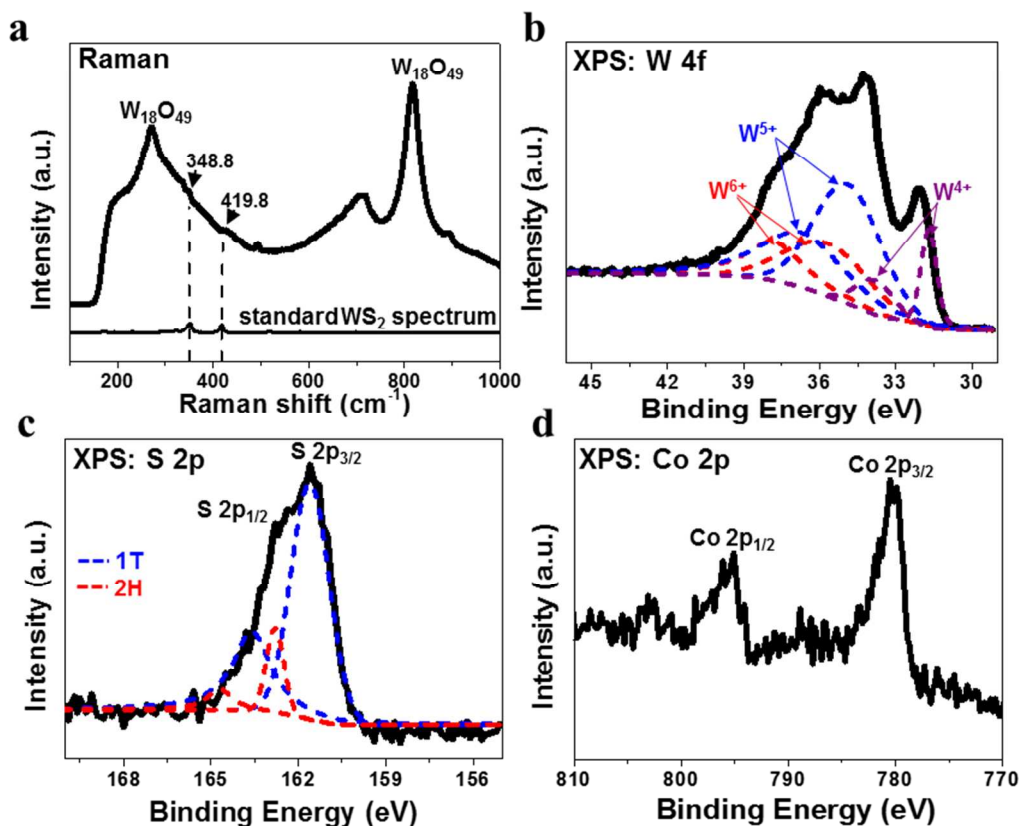


Figure 4. Raman and XPS spectra of the optimized Co:WS₂/Co:W₁₈O₄₉ core/shell nanotubes. (a) Raman spectra show dominant W₁₈O₄₉ peaks with tiny humps corresponding to WS₂. XPS spectra of W 4f (b), S 2p (c) and Co 2p (d) peaks, confirming the existence of Co doping and S. The S 2p peaks indicate that there is a mixture of 2H- and 1T-phase WS₂ on the surface. All results are shown for the best condition identified in this work (Co/(Co+W)=15%).

Optimal Performance of WS₂/doped WS₂ on FTO			
Reference, Catalyst	Current Density (J) @ -0.4V vs. RHE	Area used to calculated Current Density J	η_{-10}
This work	-37mA/cm²	Geometric area of FTO (1.5 cm ²)	0.24V
WS ₂ /graphene ³⁹	-25mA/cm²	Geometric area of FTO; (size unspecified)	0.33V
Amorphous Ni:WS ₂ ⁴¹	-29mA/cm²	Geometric area of FTO (0.25 cm ²)	0.28V
WS ₂ film ¹⁰	-6 mA/cm²	Geometric area of FTO; (size unspecified)	0.55V
WS ₂ Bulk ⁴³	-2mA/cm²	Geometric area of FTO; (size unspecified)	>0.7V
WS ₂ Nanoflakes ⁴³	-16mA/cm²	Geometric area of FTO; (size unspecified)	0.36V
Exfoliated bulk WS ₂ ⁴⁴	0.5mA/cm²	Geometric area of FTO (1.0 cm ²)	>1.0V

Table 1. HER performance summary of various forms of WS₂ supported on FTO substrates to show the Co doping effect in this work. η_{-10} refers to the overpotential at -10mA/cm² normalized to the geometric area.

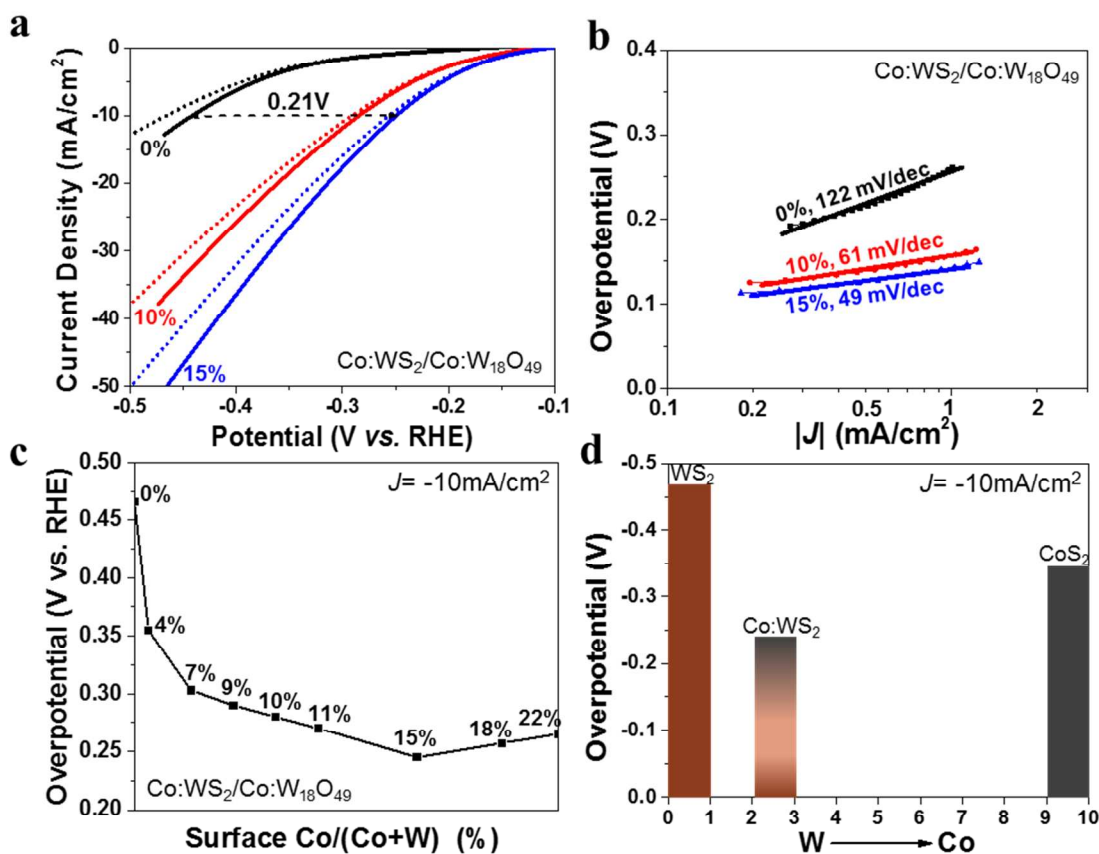


Figure 5. Electrochemical performance comparison for HER. (a) J - V curves of three representative conditions of pristine WS₂/W₁₈O₄₉ (0%) and Co doped ones (10%, 15%). The dotted and solid lines correspond to before and after iR correction; (b) Corresponding Tafel plots; (c) The overpotential for achieving -10 mA/cm² of Co:WS₂/Co:W₁₈O₄₉ nanotubes as a function of surface Co atomic percentage for Co and W; (d) Overpotential for achieving -10 mA/cm² for undoped WS₂, pure CoS₂, and optimal Co:WS₂ shells on W₁₈O₄₉ nanotube cores.

EE-ART-04-2018-001111.R1

Title: Rapid Flame Doping of Co to WS₂ for Efficient Hydrogen Evolution

Authors: Xinjian Shi, Meredith Fields, Joonsuk Park, Joshua M. McEnaney, Hongping Yan, Yirui Zhang, Charlie Tsai, Thomas F. Jaramillo, Robert Sinclair, Jens K. Nørskov, Xiaolin Zheng

Broader context

Hydrogen is a clean fuel for fuel cells and an energy carrier. Producing hydrogen by water electrolysis can further leverage the rapid growth of renewable energy resources, such as solar and wind. A critical economical barrier for water electrolysis is to develop earth abundant catalyst for hydrogen evolution reaction (HER) to replace the noble metal catalyst Pt.

In this context, transition metal sulfides, such as MoS₂ and WS₂, have been extensively investigated as a promising HER catalyst, but their catalytic performance remains inferior than Pt. One strategy to further improve their activity is to dope transition metal sulfides, but the dopants typically end up at the edges, leaving the vast basal plane unutilized. Here, we first synthesized Co doped W₁₈O₄₉ nanotubes and then sulfurized the oxides to Co:WS₂. This approach also enables to investigate the doping concentration effect for HER. Our optimal Co doped WS₂ shows the best hydrogen evolution performance among any other form of WS₂ reported using the same FTO substrate. Importantly, the overpotential reduction from Co doping for WS₂ in this work is superior to many other doped transition metal sulfides beyond WS₂.